

QUIESCENT COMPACT GALAXIES AT INTERMEDIATE REDSHIFT IN THE COSMOS FIELD II. THE FUNDAMENTAL PLANE OF MASSIVE GALAXIES

H. JABRAN ZAHID¹, IVANA DAMJANOV², MARGARET J. GELLER¹ & IGOR CHILINGARIAN^{1,3}

¹Smithsonian Astrophysical Observatory, 60 Garden St., Cambridge, MA 02138, USA

²Harvard-Smithsonian Center for Astrophysics - 60 Garden Street, Cambridge, MA 02138 and

³Sternberg Astronomical Institute, Moscow State University, 13 Universitetsky prospect, 119992 Moscow, Russia

Draft version July 4, 2018

ABSTRACT

We examine the relation between surface brightness, velocity dispersion and size—the fundamental plane—for quiescent galaxies at intermediate redshifts in the COSMOS field. The COSMOS sample consists of ~ 150 massive quiescent galaxies with an average velocity dispersion $\sigma \sim 250 \text{ km s}^{-1}$ and redshifts between $0.2 < z < 0.8$. More than half of the galaxies in the sample are compact. The COSMOS galaxies exhibit a tight relation (~ 0.1 dex scatter) between surface brightness, velocity dispersion and size. At a fixed combination of velocity dispersion and size, the COSMOS galaxies are brighter than galaxies in the local universe. These surface brightness offsets are correlated with the rest-frame $g - z$ color and D_n4000 index; bluer galaxies and those with smaller D_n4000 indices have larger offsets. Stellar population synthesis models indicate that the massive COSMOS galaxies are younger and therefore brighter than similarly massive quiescent galaxies in the local universe. Passive evolution alone brings the massive compact quiescent COSMOS galaxies onto the local fundamental plane at $z = 0$. Therefore, evolution in size or velocity dispersion for massive compact quiescent galaxies since $z \sim 1$ is constrained by the small scatter observed in the fundamental plane. We conclude that massive compact quiescent galaxies at $z \lesssim 1$ are not a special class of objects but rather the tail of the mass and size distribution of the normal quiescent galaxy population.

Subject headings: galaxies: evolution – galaxies: high-redshift – galaxies: formation – galaxies: structure

1. INTRODUCTION

Observations of the structural properties of galaxies across cosmic time are critical for understanding how galaxies form and evolve. Most massive galaxies observed in the universe are not actively forming stars, i.e. they are quiescent. Quiescent galaxies exist at $z \sim 4$ (Fontana et al. 2009) and begin to dominate the massive galaxy population at $z = 2 \sim 3$ (Ilbert et al. 2013; Muzzin et al. 2013). The massive quiescent galaxies observed at $z \sim 2$ have effective radii that are on average smaller than the local massive quiescent galaxy population (Daddi et al. 2005; Trujillo et al. 2007; Zirm et al. 2007; Toft et al. 2007; Buitrago et al. 2008; van Dokkum et al. 2008; Damjanov et al. 2011; van der Wel et al. 2014). It is not clear whether the observed average size growth of quiescent galaxies since $z \sim 2$ is due to the growth of individual galaxies (e.g., Cimatti et al. 2008; Taylor et al. 2010) or to the addition of larger galaxies to the quiescent galaxy population at later times (e.g., Valentinuzzi et al. 2010; Cassata et al. 2011, 2013; Carollo et al. 2013).

Several theoretical scenarios have been proposed to explain the origin and evolution of massive compact quiescent (MCQ) galaxies. Compact galaxies may form at $z \gtrsim 2$ from gas-rich major mergers (Khochfar & Silk 2006) and/or instabilities in clumpy disks (Elmegreen et al. 2008; Dekel & Burkert 2014). At late times they may also form from tidal interactions (Bekki et al. 2001; Chilingarian et al. 2009). They can grow in size through minor mergers and accretion (van der Wel et al. 2009; Naab et al. 2009; Shih & Stockton 2011; Newman et al. 2012) and/or feedback driven adiabatic expansion

(Fan et al. 2008, 2010). These growth mechanisms are evoked to account for both the larger average size of quiescent galaxies today as compared to $z \sim 2$ and the putative dearth of MCQ galaxies in the local universe.

The number density of MCQ galaxies in the local universe probed by Sloan Digital Sky Survey (SDSS) is apparently 2-3 orders of magnitude smaller than at $z \sim 1-2$ (Trujillo et al. 2009; Taylor et al. 2010). These estimates are consistent with an evolutionary scenario where MCQ galaxies form at high redshift and the number density rapidly declines as they grow in size since $z \sim 1$ (e.g. van Dokkum et al. 2010; Newman et al. 2012). However, number density estimates of MCQ galaxies in dense regions in the local universe (Valentinuzzi et al. 2010; Poggianti et al. 2013) and some studies at intermediate redshifts (Carollo et al. 2013; Damjanov et al. 2014; Damjanov et al. 2015, submitted, hereafter Paper I) find no rapid decline. Instead, these studies show that the number density of MCQ galaxies remains roughly constant since $z \sim 1$. Thus, MCQ galaxies may not significantly grow in size since $z < 1$ or they may be produced at a rate that compensates for their growth. The relation between structural and kinematic properties of MCQ galaxies may provide important clues for understanding their origin and evolution. Here we examine the fundamental plane, i.e. the relation between surface brightness, central velocity dispersion and effective radius, for a sample of MCQ galaxies at $0.2 < z < 0.8$.

Galaxies in virial equilibrium show a relation between luminosity, size and velocity dispersion. Djorgovski & Davis (1987) and Dressler et al. (1987) first demonstrated that quiescent galaxies in the lo-

cal universe exhibit a tight correlation between surface brightness, effective radius and velocity dispersion—the fundamental plane (FP). The scatter in the FP is small (~ 0.05 dex; Bernardi et al. 2003; Saulder et al. 2013) and the FP appears to extend across all early-type galaxies in the local universe (Misgeld & Hilker 2011).

The physical basis of the FP is the virial equilibrium of stellar systems dynamically supported by random motions. The observed properties of surface brightness, effective radius and velocity dispersion serve as proxies for the virial mass density, virial radius and virial velocity, respectively. As such, the FP is tilted relative to the expected virial relation (e.g., Bernardi et al. 2003) and the FP evolves with redshift (Treu et al. 2005; Holden et al. 2010; Saglia et al. 2010; Fernández Lorenzo et al. 2011; van de Sande et al. 2014). Some of the evolution observed in the FP may possibly be attributed to evolution in the ratio between stellar and dynamical mass (Beifiori et al. 2014; Peralta de Arriba et al. 2014), though this is not the dominant effect.

We examine the fundamental plane for massive compact quiescent galaxies at $z < 1$. In Section 2 we describe the data and methods and Section 3 contains the results. We discuss the results in Section 4 and we conclude in Section 5. We adopt the standard cosmology $(H_0, \Omega_m, \Omega_\Lambda) = (70 \text{ km s}^{-1} \text{ Mpc}^{-1}, 0.3, 0.7)$, AB magnitudes and a Chabrier (2003) IMF.

2. DATA AND METHODS

2.1. Data Selection

We examine galaxies in the 1.6 deg^2 COSMOS field (Scoville et al. 2007). All galaxies that we select in the COSMOS field have *HST* ACS imaging (Koekemoer et al. 2007) UV to IR multi-band photometry (Ilbert et al. 2013, and references therein) and SDSS/BOSS spectroscopy to the SDSS and BOSS survey magnitude limits of $r < 17.77$ and $i < 19.9$, respectively (Ahn et al. 2014). We cross reference objects that have structural parameters given in the morphology catalog of Sargent et al. (2007)¹, multi-band photometry from the catalog of Ilbert et al. (2013)² and SDSS/BOSS spectroscopy by position matching objects within a 0.5 arcsecond radius. We select galaxies in the intermediate redshift range $0.2 < z < 0.8$ classified as quiescent by Ilbert et al. (2013) based on a rest-frame color-color selection ($NUV - r$ versus $r - J$). These selection criteria yield a sample of 161 galaxies.

We require robust measurements of velocity dispersions in order to derive the FP. From the cross-matched sample of 161 galaxies, we select galaxies with velocity dispersions $> 70 \text{ km s}^{-1}$ and velocity dispersion errors $< 100 \text{ km s}^{-1}$. From examination of the spectra, we find that two galaxies in the sample have strong emission lines. Both galaxies exhibit emission line ratios consistent with active galactic nuclei (Baldwin et al. 1981; Kauffmann et al. 2003; Kewley et al. 2006). We remove these two galaxies from the sample. The final sample from which we derive the FP consists of 148 galaxies. We refer to this sample as the COSMOS sample.

In Section 2.3 we investigate sample selection bias. The most restrictive selection is imposed by the SDSS/BOSS spectroscopic target selection. To assess the effects of this selection, we compare the COSMOS sample of 148 galaxies with a sample of quiescent galaxies in the COSMOS field with measured spectroscopic redshifts compiled from publicly available data (Davies et al. 2015). We restrict the comparison sample to galaxies with HST size measurements, stellar masses $> 10^{10} M_\odot$ and redshifts in the range of $0.2 < z < 0.8$. This larger sample consists of 2970 galaxies.

2.2. Measured Properties

The SDSS team derives redshifts and velocity dispersions according to Bolton et al. (2012). Redshifts are determined from fitting template spectra at a range of trial redshifts. The central velocity dispersion is determined by comparing the observed spectra with model spectra which are redshifted to the galaxy redshift and convolved to the instrument resolution. Each model spectra is successively broadened to larger velocity dispersions in steps of 25 km s^{-1} . The best-fit velocity dispersion is determined by fitting for the velocity dispersion at the minimum chi-squared based on the measured chi-squared values at each 25 km s^{-1} broadening step.

We correct the velocity dispersion measured in the $2''$ (BOSS) and $3''$ (SDSS) apertures to the measured effective radius using the Jorgensen et al. (1995, see their Equation 2) correction. The median correction applied to the sample is ~ 0.04 dex. The typical error in the velocity dispersion for the COSMOS sample is $\sim 30 \text{ km s}^{-1}$. Figure 1A and 1B show the redshift and corrected velocity dispersion distribution, respectively.

To constrain the stellar population age, we measure the D_n4000 index directly from the SDSS spectra. The D_n4000 index is an age sensitive spectral feature defined as the ratio of flux in two spectral windows adjacent to the 4000\AA break (for definition see Balogh et al. 1999).

The effective radii of galaxies in the COSMOS sample are measured from *HST* ACS imaging by Sargent et al. (2007). The $\lesssim 0.1''$ *HST* resolution corresponds to a physical length of $\lesssim 0.7 \text{ kpc}$ at $z \sim 0.75$. Sargent et al. (2007) fit each surface brightness profile with a single Sersic (1968) profile model using GIM2D (Simard et al. 2002). The formal uncertainty on size is typically $\lesssim 0.005$ dex. Because these errors are small, we ignore the uncertainty in size. We correct the measured semi-major half-light radius to the circularized averaged half-light (effective) radius given by

$$R_e = a_{50} \sqrt{\frac{b}{a}} \quad (1)$$

where a_{50} is the semi-major half-light radius and $\frac{b}{a}$ is the semi minor-to-major axis ratio. van der Wel et al. (2014) find that galaxy sizes depend on the wavelength of observation. In order to compare with the local g -band FP, we correct the galaxy sizes to the rest-frame g -band effective wavelength ($\lambda = 4686\text{\AA}$; Stoughton et al. 2002), using the correction given by van der Wel et al. (2014, see their Equation 2). The circularized and color corrected radius is typically ~ 0.04 dex smaller on average than the measured semi-major effective radius. This correction does not change any of the major conclusions of

¹ http://irsa.ipac.caltech.edu/data/COSMOS/tables/morphology/cosmos_morph_zurich_1.0.tbl

² <http://vizier.cfa.harvard.edu/viz-bin/VizieR?-source=J/A+A/556/A55>

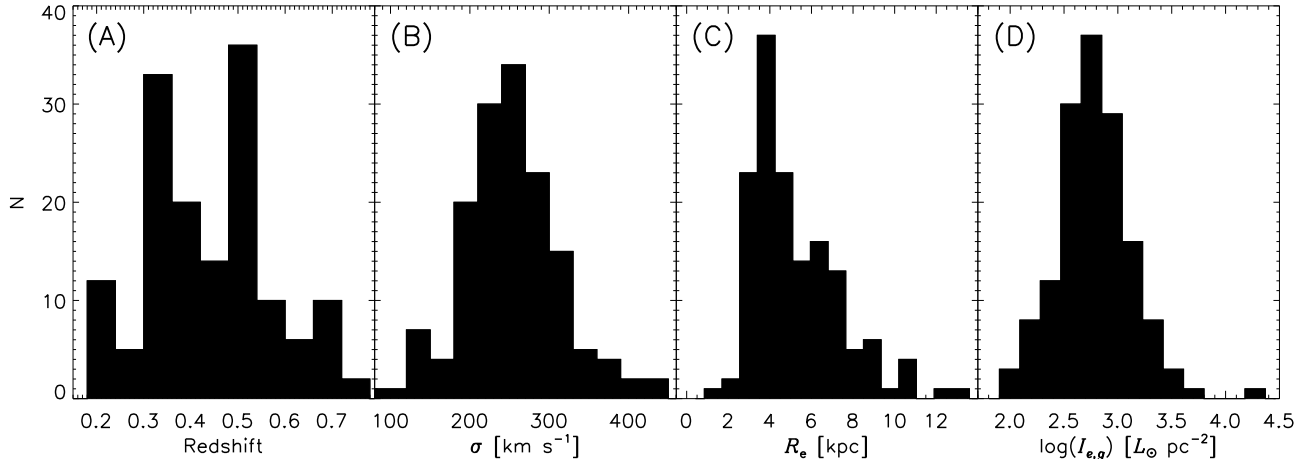


FIG. 1.— (A) Redshift, (B) velocity dispersion, (C) circularized half-light radius and (D) surface brightness distribution of the 148 galaxies in the COSMOS sample.

this work. In Figure 1C we show the corrected effective radius distribution for the COSMOS sample.

We determine the surface brightness in the SDSS rest-frame g, r, i, z -bands by synthesizing photometry in these bands from the measured multi-band UV to IR SED. We determine k -corrected and reddening corrected magnitudes by fitting stellar population synthesis models of Bruzual & Charlot (2003) to the observed spectral energy distribution using the LePHARE³ code written by Arnout S. & Ilbert O. (for details see Arnouts et al. 1999; Ilbert et al. 2006).

The surface brightness in mag arcsec^{-2} is

$$\mu_e = m + 5 \log(r_e) + 2.5 \log(2\pi) - 10 \log(1 + z), \quad (2)$$

where m is the reddening and k -corrected magnitude, r_e is the radius measured in arcseconds and the final term is the cosmological surface brightness dimming correction. We convert the surface brightness to I_e , measured in $L_\odot \text{pc}^{-2}$ using

$$\log\left(\frac{I_e}{L_\odot \text{pc}^{-2}}\right) = 0.4 \left(M_\odot + 21.572 - \frac{\mu_e}{\text{mag arcsec}^{-2}} \right), \quad (3)$$

where $M_\odot = 5.12^4$ is the g -band solar absolute magnitude. The stellar mass in LePHARE represents the scale factor between the best-fit SED and the observed luminosity; the error estimate accounts for observational and some systematic uncertainties associated with the SED fitting procedure. The typical observational uncertainty on stellar masses is $\lesssim 0.1$ dex, though the systematic errors may be larger (e.g. Conroy & Gunn 2010). We adopt 0.1 dex as the error estimate on surface brightness. In Figure 1D we show the surface brightness distribution of the COSMOS sample. The results are independent of the photometric band. For ease of comparison with previous results, the analysis and results are based on the rest-frame g -band surface brightness. We give the measured and derived sample properties in Table 1.

For the local benchmark, we compare with the orthogonal fit FP derived by Hyde & Bernardi (2009, HB09

hereafter) using $\sim 50,000$ galaxies in the SDSS. We anticipate that some of the evolution in the FP is due to passive evolution of galaxies (e.g., Treu et al. 2005) so we rewrite the HB09 FP in terms of surface brightness

$$\log(I_{e,g}) = A \log(\sigma_e) + B \log(R_e) + C. \quad (4)$$

Here, σ_e and R_e are measured in km s^{-1} and kpc, respectively. We convert the FP parameters from HB09 into surface brightness units of $L_\odot \text{pc}^{-2}$. The best-fit parameters for the local g -band FP are $A = 1.84$, $B = 1.31$ and $C = 0.96$.

There is no single definition for compact galaxies. We identify galaxies as compact using the Barro et al. (2013) classification:

$$\log\left(\frac{M_*}{R_e^{1.5}}\right) \geq 10.3 M_\odot \text{kpc}^{-1.5}. \quad (5)$$

Here, M_* is the stellar mass in solar mass units. We adopt the stellar mass estimate given in the Ilbert et al. (2013) catalog. Using this definition, 57% (85/148) of the galaxies in Table 1 are compact.

2.3. Sample Bias

Figure 2A shows the surface brightness distribution as a function of size for the COSMOS sample (blue stars) relative to a similarly selected comparison sample (black points; see Section 2.1 for details of sample selection). The COSMOS sample is biased towards the largest galaxies and at a fixed size the selected sample populates the high surface brightness envelope of the full sample distribution. Figures 2B and 2C show the absolute g -band magnitude and size as a function of redshift, respectively. The brightest and largest objects are selected across the redshift range. The COSMOS sample is subject to the SDSS/BOSS target selection and the limits of SDSS/BOSS spectroscopy; the SDSS/BOSS target selection criteria lead to a selection bias towards high surface brightness galaxies. Furthermore, as expected, Figure 2B shows that increasingly brighter galaxies are selected with increasing redshift. Because of the SDSS/BOSS target selection, the galaxies in the COSMOS sample are drawn from the massive, high surface brightness tail of

³ <http://www.cfht.hawaii.edu/~arnouts/LEPHARE/lephare.html>

⁴ <http://classic.sdss.org/dr5/algorithms/sdssUBVRITransform.html>

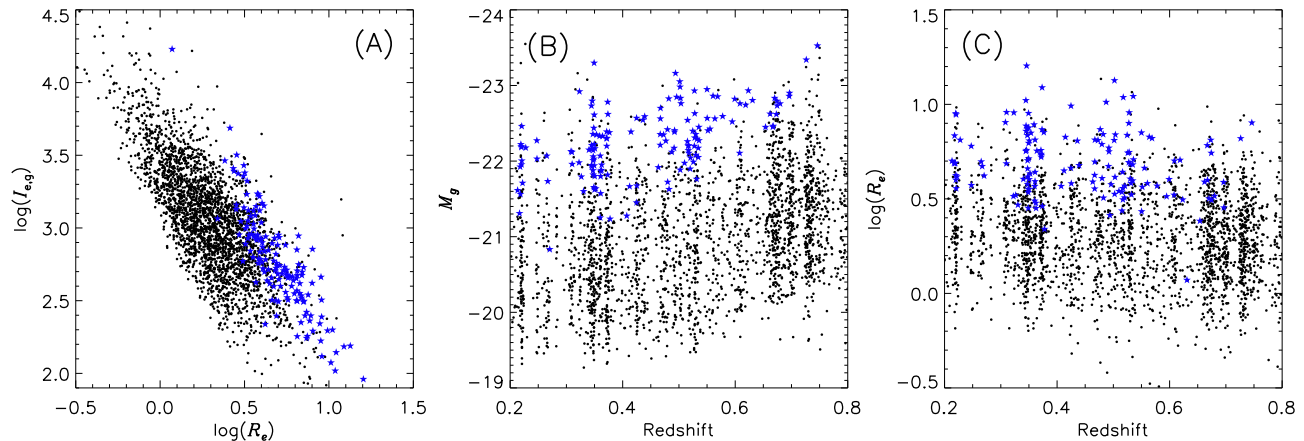


FIG. 2.— (A) Surface brightness as a function of size, (B) absolute g -band magnitude as a function of redshift and (C) size as a function of redshift. The blue stars and black points are the 148 galaxies in the COSMOS sample and the comparison sample of quiescent galaxies, respectively (see Section 2.1).

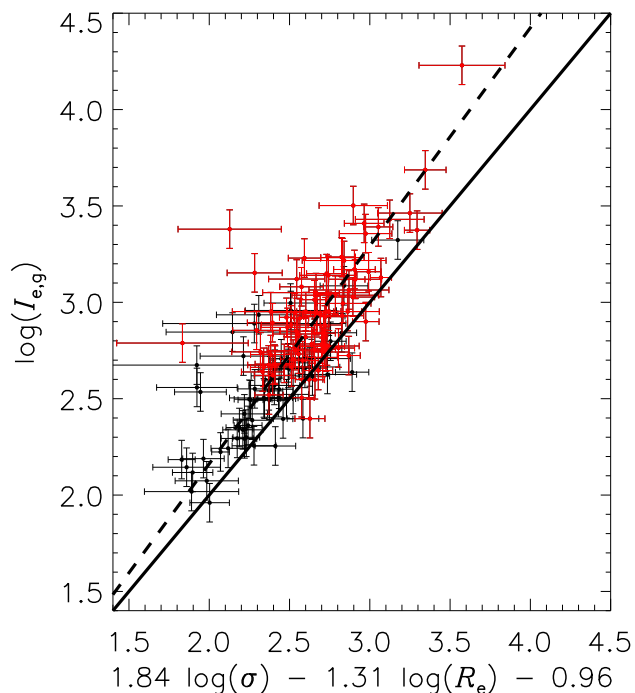


FIG. 3.— Fundamental plane for the COSMOS sample. The solid line is the HB09 relation; the dashed line is the best fit FP for the COSMOS sample. The red points are compact galaxies.

the quiescent galaxy distribution. The selection bias results in a large fraction of compact galaxies in the COSMOS sample.

3. RESULTS

3.1. The Fundamental Plane

Figure 3 shows the relation between velocity dispersion, effective radius and surface brightness for the 148 galaxies in the COSMOS sample. The red points indicate compact galaxies (see Equation 5). The compact galaxies in the sample typically have higher surface brightness, higher velocity dispersion and smaller size. Thus, they populate the upper right hand part of the figure. The

solid line is the local relation from HB09.

The data show a clear offset from the local relation; for a given velocity dispersion and effective radius, galaxies in the COSMOS sample are brighter than local galaxies. The dashed line is a fit to the data (Equation 4). The fit is an orthogonal regression implemented in the *saxlin.pro* IDL routine in the astronomy users library. The best-fit parameters are $A = 2.09 \pm 0.12$, $B = -1.49 \pm 0.09$ and $C = -1.19 \pm 0.07$. The errors are based only on the dispersion of the data and do not account for observational uncertainties.

3.2. Quiescent Evolution

Here we demonstrate that the surface brightness offsets of COSMOS galaxies relative to the local galaxy population (Figure 3) can be explained by simple quiescent evolution. We define the surface brightness offsets as the difference between the observed galaxy surface brightness of the COSMOS sample and the surface brightness calculated from the best-fit local FP:

$$\Delta \log(I_{e,g}) = \log(I_{e,m}) - [A \log(\sigma_{e,m}) + B \log(R_{e,m}) + C]. \quad (6)$$

Here, $I_{e,m}$, $\sigma_{e,m}$ and $R_{e,m}$ are the measured surface brightness, velocity dispersion and effective radius for the COSMOS sample and A , B and C are best-fit local FP parameters taken from HB09 (see Section 2).

A rank correlation shows that the FP offsets, $\Delta \log(I_{e,g})$, are correlated with redshift (6.8σ significance), the rest-frame $g-z$ color⁵ (6.5σ significance), and D_n4000 index (3.4σ significance). Bluer galaxies with smaller D_n4000 indices have larger surface brightness offsets. Both the rest-frame $g-z$ color and the D_n4000 index are also correlated with redshift; galaxies at higher redshifts are bluer and have smaller D_n4000 index. These trends are consistent with the simple interpretation that at a fixed combination of velocity dispersion and size, the higher redshift galaxies in the COSMOS sample are younger and therefore brighter and bluer than their local counterparts. The SDSS/BOSS target selection partly

⁵ The offsets are strongly correlated with other rest-frame colors (i.e. $g-r$, $g-i$ and $r-i$) in the same sense; bluer galaxies show larger offsets.

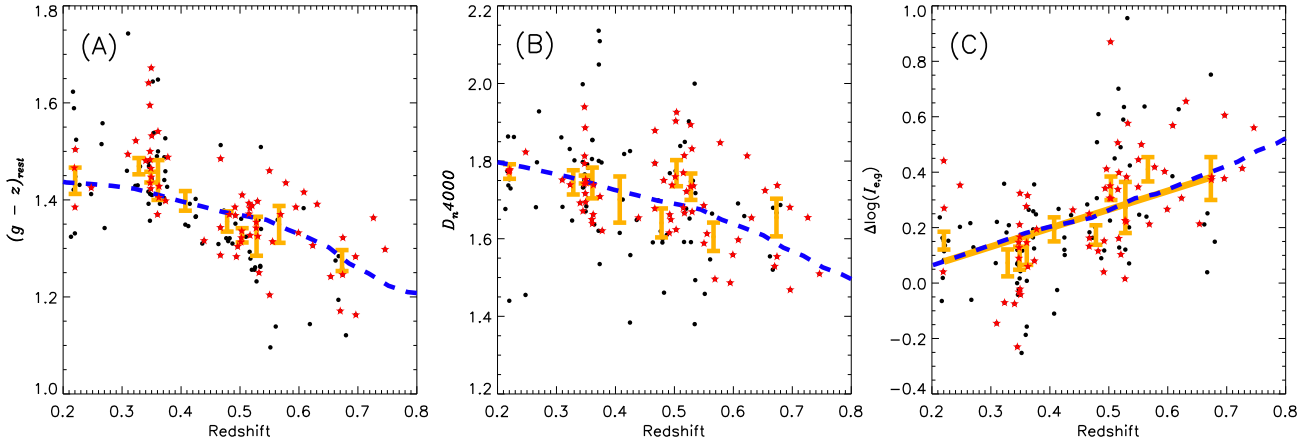


FIG. 4.— (A) Rest-frame $g - z$ color, (B) D_n4000 index and (C) FP offsets for the COSMOS sample as a function redshift. The black points and red stars are the individual galaxies in the COSMOS sample and the red stars denote compact galaxies. The orange points are the median (A) rest-frame $g - z$ color, (B) D_n4000 index and (C) FP offsets in 10 equally populated bins of redshift. The errors bars are bootstrapped. The dashed blue curves show a model of a passively evolving galaxy where star formation began at $z \sim 1.7$ and ceased at $z \sim 1.3$. The solid orange line in (C) is a linear fit to the binned data.

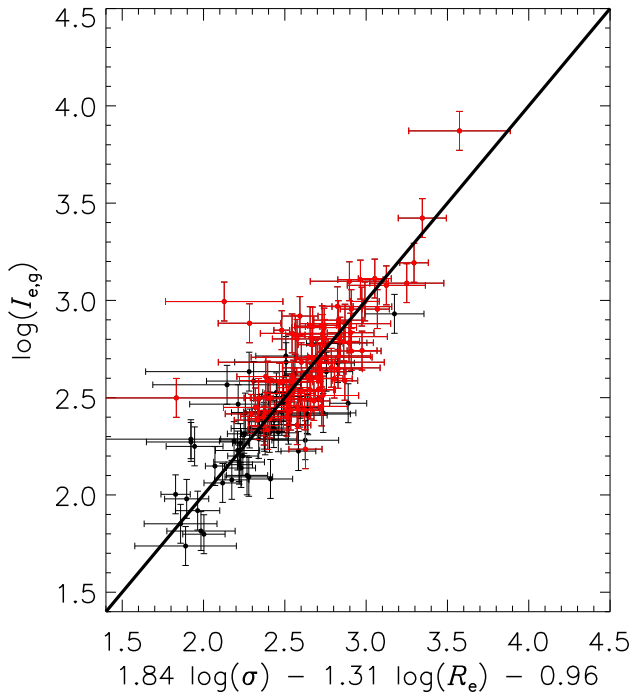


FIG. 5.— Zero redshift fundamental plane accounting for quiescent evolution of the COSMOS sample. The solid line is the local fundamental plane relation from HB09. The red points are compact galaxies.

contributes to these trends (see Section 2.3) Thus mere quiescent evolution contributes to the observed offset between the COSMOS sample and the local FP.

The luminosity of a quiescent galaxy decreases as it passively evolves. To quantify this effect, we model a passively evolving galaxy using the Flexible Stellar Population Synthesis (FSPS) model (Conroy et al. 2009; Conroy & Gunn 2010). FSPS generates both synthetic photometry and spectra as a function of time for an input star formation and metallicity history. We model

both the g -band luminosity and the rest-frame $g - z$ color of a passively evolving galaxy based on synthetic magnitudes matched to the SDSS filters. We calculate the D_n4000 index directly from the synthetic spectra which have spectral resolution comparable to the SDSS. We model a galaxy with constant star formation rate of $\sim 400 M_\odot \text{ yr}^{-1}$ for 1 Gyr at solar metallicity. The star formation rate is set to match the median stellar mass of the COSMOS sample. For a constant metallicity and constant and continuous star formation history, evolution of the $g - z$ color, D_n4000 index and the relative evolution of the luminosity only depend on the duration of star formation. We tried star formation histories that spanned 0.5 - 2 Gyr in duration with similar results. The only free parameter in the model is the formation redshift.

We constrain the formation redshift of the model galaxy by fitting the median rest-frame $g - z$ color and D_n4000 index distribution of the COSMOS sample. Figures 4A and 4B show the rest-frame $g - z$ color and D_n4000 index as a function of redshift, respectively. In each panel the black points and red stars are the respective properties of individual galaxies in the COSMOS sample. The orange points are the median of the respective properties in 10 equally populated bins of redshift and the errors are bootstrapped. The dashed blue curves show the FSPS model. The rest-frame $g - z$ color and D_n4000 index distributions of the COSMOS sample are broadly consistent with a passively evolving galaxy which began star formation at $z \sim 1.7$ and ceased star formation at $z \sim 1.3$. This redshift interval corresponds to 1 Gyr.

Figure 4C shows the FP offsets, $\Delta \log(I_{e,g})$, as a function of redshift. The black points and red stars are FP offsets for individual galaxies in the COSMOS sample and the orange points are the median of the FP offsets in 10 equally populated bins of redshift. The errors are bootstrapped. The solid orange line is a fit to the median data:

$$\Delta \log(I_{e,g}) = (-0.071 \pm 0.049) + (0.67 \pm 0.12)z. \quad (7)$$

The bootstrapped errors on the median are propagated through to the fit parameters. We refer to this relation as the luminosity evolution correction. The dashed blue curve is the g -band luminosity of the FSPS model galaxy normalized to the median g -band luminosity of the COSMOS sample $L_g \sim 10^{10.9} L_\odot$. The FP offsets plotted in Figure 4C are relative to the local relation. The consistency between the change in luminosity of a passively evolving galaxy and the FP offsets means that passive luminosity evolution alone accounts for the offset between the FP we derive from the COSMOS data and the local FP from HB09 (dashed and solid line in Figure 3, respectively).

To demonstrate that passive evolution alone is sufficient to explain the offset of the COSMOS sample from the local FP, we apply the luminosity evolution correction given by Equation 7 to the data. We emphasize that this evolution correction is consistent with the luminosity evolution of a passively evolving galaxy which ceased star-formation at $z \sim 1.3$ (see Figure 4C). Figure 5 shows the FP for the COSMOS sample brought to $z = 0$ by accounting for the quiescent luminosity evolution shown in Figure 4. The scatter of the data in Figure 5 is ~ 0.15 dex. Based on the observational uncertainties in velocity dispersion (~ 0.07 dex) and luminosity (~ 0.1 dex) the intrinsic scatter is $\lesssim 0.1$ dex. The luminosity corrected data are consistent with the local FP. Passive evolution of galaxies in the COSMOS sample is sufficient to place them on the local FP by $z \sim 0$.

4. DISCUSSION

We examine the FP for a sample of galaxies spanning the redshift range of $0.2 < z < 0.8$. Due to the strong selection bias towards high surface brightness objects, MCQ galaxies comprise a large fraction of the COSMOS sample we examine. Passive evolution alone brings the COSMOS sample onto the local FP by $z = 0$. The physical basis of the fundamental plane is the virial equilibrium of quiescent galaxies. Thus we conclude that MCQ galaxies are virialized systems.

Several studies examining the FP at intermediate and high redshifts have recognized the importance of evolution of stellar populations. Treu et al. (2005) report that offsets from the fundamental plane for galaxies in the redshift range of $0.2 < z < 1.2$ are anti-correlated with stellar mass; lower mass galaxies have larger offsets. They attribute these trends to downsizing. Lower mass galaxies are younger and therefore have smaller mass-to-light (M/L) ratios. To account for evolution of stellar populations and varying M/L ratios, Bezanson et al. (2013) derive the “mass” FP substituting stellar mass surface density for surface brightness. In contrast to the observed offsets in the FP, they find very small offset between the mass FP at $z \sim 2$ and the local relation. van de Sande et al. (2014) quantify the evolution of the zero-point of the FP out to $z \sim 2$. They find that $\Delta \log(M/L_g) \propto (-0.49 \pm 0.03)z$.

We conclude that the FP offsets are due to the evolution of stellar populations. In particular, we find that passive evolution alone can bring galaxies in the COSMOS sample onto the local FP relation. Thus, $\Delta \log(I_{e,g}) = -\Delta \log(M/L_g)$. Based on comparisons of our data with stellar population synthesis models, we determine that $\Delta \log(I_{e,g}) \propto (0.69 \pm 0.12)z$ (see Equation

7). The evolution we measure is consistent (1.5σ) with evolution reported by van de Sande et al. (2014, also see references therein). We note however that both studies are biased towards bluer objects and therefore the reported evolution may not be representative of the quiescent galaxy population. In general, our results are qualitatively consistent with previous studies examining the evolution of the FP. The novel aspect of this work is that it demonstrates that MCQ galaxies follow the same evolutionary trends as the general quiescent galaxy population.

Due to the SDSS/BOSS target selection, COSMOS galaxies examined in this study are outliers in the relation between stellar mass and size. However, the stellar population and kinematics of MCQ galaxies in the COSMOS sample are consistent with the local quiescent galaxy population. Thus, we conclude that MCQ galaxies at $0.2 < z < 0.8$ represent the extreme of the mass and size distribution of normal quiescent galaxies (see Figure 2) and are not a unique class of objects. Saulder et al. (2015) reach similar conclusions based on a larger sample culled from the literature.

Recent cosmological hydrodynamical simulations suggest that compact galaxies at $z \sim 2$ do not form from unique physical mechanisms but rather are subject to the same formation processes as other galaxies (Wellons et al. 2014). Thus, both the origin and evolution of MCQ galaxies appear to be consistent with the conclusion that compact galaxies are the tail of the normal galaxy distribution.

If MCQ galaxies at $z < 1$ passively evolve with little or no size growth, their descendants should be identifiable among the local galaxy population. However, the number density evolution of compact galaxies since $z \sim 1$ remains unsettled. Several studies based on the SDSS claim that the number density of compact galaxies drops dramatically in the local universe (e.g. Shen et al. 2003; Trujillo et al. 2009; Taylor et al. 2010; Cassata et al. 2013). This has led to the suggestion that they grow significantly since $z \sim 1 - 2$. If this is the case, the small scatter in the FP at $z < 1$ means that any growth mechanism ostensibly moves galaxies along, not off, the FP. Additionally, if galaxies do grow in size, the results of this study provide empirical constraints for theoretical analysis of galaxy growth (see for example Hopkins et al. 2010). However, it is possible that compact galaxies today are preferentially found in environments that are incompletely sampled by the SDSS (see Taylor et al. 2010). Thus their number densities may be systematically underestimated in the local universe.

In contrast to studies reporting a rapid decline in the number density of compact galaxies at $z < 1$, several studies find that the number density remains roughly constant (e.g., Valentinuzzi et al. 2010; Poggianti et al. 2013; Carollo et al. 2013; Damjanov et al. 2014). The results of our companion paper (Paper I) are consistent with this conclusion. In this case, either galaxies do not grow in size or compact galaxies are produced at a rate that compensates for their growth.

Carollo et al. (2013) conclude that evolution in the mass-size relation is dominated by newly formed quiescent galaxies, i.e. progenitor bias. They argue that a scenario where individual galaxies grow and new compact galaxies form at $z < 1$ is inconsistent with the fact that

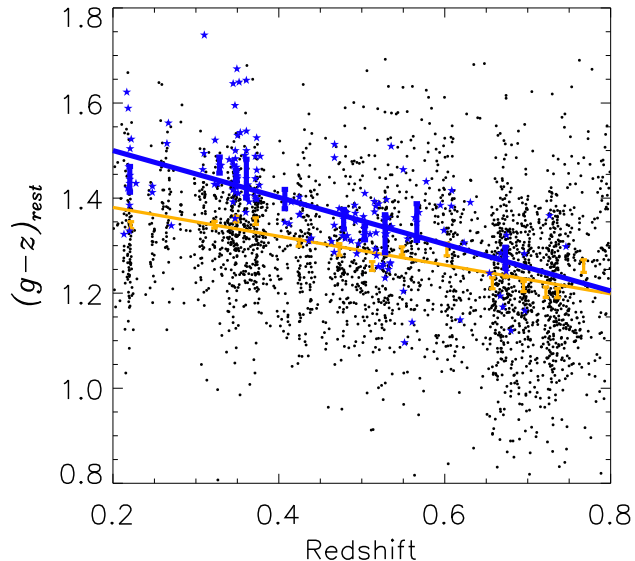


FIG. 6.— Rest-frame $g - z$ color as a function of redshift for the COSMOS sample (blue stars) and the comparison sample (black points). The blue and orange points are the median rest-frame $g - z$ color in equally populated bins of redshift and the blue and orange lines are fits to the median color for the COSMOS sample and the comparison sample, respectively. The error bars are bootstrapped.

compact galaxies are systematically redder at lower redshifts suggesting that the population is aging over time and that the normal quiescent galaxy population is bluer than compact galaxies indicating that the regular population has more recently shutdown star formation as compared to the compact population.

Figure 6 compares the rest-frame $g - z$ color of the selected COSMOS sample, dominated by MCQ galaxies, with the comparison COSMOS sample (see Section 2.1 for sample description). The data are broadly consistent with the interpretation of Carollo et al. (2013). MCQ galaxies are redder at late times and redder than the normal quiescent galaxy population. However, we note that the scatter in the rest-frame $g - z$ color and D_n4000 index is large; there are galaxies in the selected COSMOS sample that have colors and D_n4000 indices consistent with younger stellar populations. A combination of progenitor bias *and* individual galaxy growth may be the basis for the evolution of the mass-size relation. Moreover, given the strong selection bias in the selected COSMOS sample, we probe only the extreme end of the mass distribution. Spectroscopically complete samples at $z < 1$ will provide important constraints for the role of progenitor bias and individual galaxy growth in the evolution of the mass-size relation.

Comparison of the COSMOS sample with a model of a passively evolving galaxy shows that, on average, the data are consistent with a galaxy which formed stars from $z \sim 1.7$ to $z \sim 1.3$. However, we emphasize the galaxies in the COSMOS sample span a broad range of ages and star formation histories contributing to the large scatter in the rest-frame $g - z$ color and D_n4000 index (Figure 4A and 4B, respectively). The best-fit $z = 1.7$ formation redshift is the average formation redshift of the sample.

Figure 5 shows that once we apply the evolutionary correction to luminosity given by Equation 7, the FP we derive from the COSMOS sample is consistent with the local relation. However, we have applied only an average correction for evolution which does not account for stellar population variations amongst galaxies at any particular redshift and the scatter in Figure 4 highlights the fact that quiescent galaxies are a heterogeneous population. The selection bias of our sample complicates the analysis of any residual offsets between our evolved sample and the local FP (Figure 5). A complete spectroscopic sample combined with sophisticated modeling of individual galaxies will allow for more robust and detailed kinematic studies.

5. SUMMARY AND CONCLUSIONS

We examine the relation between surface brightness, velocity dispersion and size—the fundamental plane—for a sample of massive compact quiescent galaxies in the COSMOS field spanning the redshift range of $0.2 < z < 0.8$. Based on analysis of this COSMOS sample, we show that:

- Massive compact galaxies at $z \lesssim 1$ populate a tight fundamental plane relation similar to the general population of quiescent galaxies in the local universe. This reflects the fact that massive compact galaxies are in virial equilibrium.
- We compare the COSMOS sample to a model of a passively evolving galaxy. The average properties of the COSMOS sample are consistent with a galaxy which started star formation at $z \sim 1.7$ and ceased star formation at $z \sim 1.3$. Accounting for passive evolution of the surface brightness brings the COSMOS sample onto the $z = 0$ fundamental plane.
- The data suggest that massive compact quiescent galaxies at $z < 1$ are not a special class of objects; they are the high mass, high surface brightness tail of the normal quiescent galaxy population.

In Paper I we show that the number density of compact galaxies remains constant for $z < 1$. This study (Paper II) concludes that the compact galaxy population is the tail of the normal galaxy population. These studies taken together demonstrate the potential of combining abundance, structural and kinematic analyses for investigating the origin and evolution of the quiescent galaxy population.

We thank the anonymous referee for their careful reading of the manuscript. HJZ gratefully acknowledges the generous support of the Clay Postdoctoral Fellowship. ID is supported by the Harvard College Observatory Menzel Fellowship and the Natural Sciences and Engineering Research Council of Canada Postdoctoral Fellowship (NSERC PDF-421224-2012). IC acknowledges support from the Russian Science Foundation project #14-22-00041. This research has made use of NASA’s Astrophysics Data System Bibliographic Services.

Funding for SDSS-III has been provided by the Alfred P. Sloan Foundation, the Participating Institutions, the

National Science Foundation, and the U.S. Department of Energy Office of Science. The SDSS-III web site is <http://www.sdss3.org/>.

SDSS-III is managed by the Astrophysical Research Consortium for the Participating Institutions of the SDSS-III Collaboration including the University of Arizona, the Brazilian Participation Group, Brookhaven National Laboratory, University of Cambridge, Carnegie Mellon University, University of Florida, the French Participation Group, the German Participation Group, Harvard University, the Instituto de Astrofísica de Canarias, the Michigan State/Notre Dame/JINA Participation Group, Johns Hopkins University, Lawrence Berke-

ley National Laboratory, Max Planck Institute for Astrophysics, Max Planck Institute for Extraterrestrial Physics, New Mexico State University, New York University, Ohio State University, Pennsylvania State University, University of Portsmouth, Princeton University, the Spanish Participation Group, University of Tokyo, University of Utah, Vanderbilt University, University of Virginia, University of Washington, and Yale University.

Based on observations made with the NASA/ESA Hubble Space Telescope, obtained at the Space Telescope Science Institute, which is operated by the Association of Universities for Research in Astronomy, Inc., under NASA contract NAS 5-26555.

REFERENCES

- Ahn, C. P., et al. 2014, *ApJS*, 211, 17
- Arnouts, S., Cristiani, S., Moscardini, L., Matarrese, S., Lucchin, F., Fontana, A., & Giallongo, E. 1999, *MNRAS*, 310, 540
- Baldwin, J. A., Phillips, M. M., & Terlevich, R. 1981, *PASP*, 93, 5
- Balogh, M. L., Morris, S. L., Yee, H. K. C., Carlberg, R. G., & Ellingson, E. 1999, *ApJ*, 527, 54
- Barro, G., et al. 2013, *ApJ*, 765, 104
- Beifiori, A., et al. 2014, *ApJ*, 789, 92
- Bekki, K., Couch, W. J., Drinkwater, M. J., & Gregg, M. D. 2001, *ApJ*, 557, L39
- Bernardi, M., et al. 2003, *AJ*, 125, 1866
- Bezanson, R., van Dokkum, P. G., van de Sande, J., Franx, M., Leja, J., & Kriek, M. 2013, *ApJ*, 779, L21
- Bolton, A. S., et al. 2012, *AJ*, 144, 144
- Bruzual, G., & Charlot, S. 2003, *MNRAS*, 344, 1000
- Buitrago, F., Trujillo, I., Conselice, C. J., Bouwens, R. J., Dickinson, M., & Yan, H. 2008, *ApJ*, 687, L61
- Carollo, C. M., et al. 2013, *ApJ*, 773, 112
- Cassata, P., et al. 2011, *ApJ*, 743, 96
- . 2013, *ApJ*, 775, 106
- Chabrier, G. 2003, *PASP*, 115, 763
- Chilingarian, I., Cayatte, V., Revaz, Y., Dodonov, S., Durand, D., Durret, F., Micol, A., & Slezak, E. 2009, *Science*, 326, 1379
- Cimatti, A., et al. 2008, *A&A*, 482, 21
- Conroy, C., & Gunn, J. E. 2010, *ApJ*, 712, 833
- Conroy, C., Gunn, J. E., & White, M. 2009, *ApJ*, 699, 486
- Daddi, E., et al. 2005, *ApJ*, 626, 680
- Damjanov, I., et al. 2011, *ApJ*, 739, L44
- Damjanov, I., Hwang, H. S., Geller, M. J., & Chilingarian, I. 2014, *ApJ*, 793, 39
- Davies, L. J. M., et al. 2015, *MNRAS*, 447, 1014
- Dekel, A., & Burkert, A. 2014, *MNRAS*, 438, 1870
- Djorgovski, S., & Davis, M. 1987, *ApJ*, 313, 59
- Dressler, A., Lynden-Bell, D., Burstein, D., Davies, R. L., Faber, S. M., Terlevich, R., & Wegner, G. 1987, *ApJ*, 313, 42
- Elmegreen, B. G., Bournaud, F., & Elmegreen, D. M. 2008, *ApJ*, 688, 67
- Fan, L., Lapi, A., Bressan, A., Bernardi, M., De Zotti, G., & Danese, L. 2010, *ApJ*, 718, 1460
- Fan, L., Lapi, A., De Zotti, G., & Danese, L. 2008, *ApJ*, 689, L101
- Fernández Lorenzo, M., Cepa, J., Bongiovanni, A., Pérez García, A. M., Ederoclite, A., Lara-López, M. A., Pović, M., & Sánchez-Portal, M. 2011, *A&A*, 526, A72
- Fontana, A., et al. 2009, *A&A*, 501, 15
- Holden, B. P., van der Wel, A., Kelson, D. D., Franx, M., & Illingworth, G. D. 2010, *ApJ*, 724, 714
- Hopkins, P. F., Bundy, K., Hernquist, L., Wuyts, S., & Cox, T. J. 2010, *MNRAS*, 401, 1099
- Hyde, J. B., & Bernardi, M. 2009, *MNRAS*, 396, 1171
- Ilbert, O., et al. 2006, *A&A*, 457, 841
- . 2013, *A&A*, 556, A55
- Jorgensen, I., Franx, M., & Kjaergaard, P. 1995, *MNRAS*, 276, 1341
- Kauffmann, G., et al. 2003, *MNRAS*, 346, 1055
- Kewley, L. J., Groves, B., Kauffmann, G., & Heckman, T. 2006, *MNRAS*, 372, 961
- Khochfar, S., & Silk, J. 2006, *ApJ*, 648, L21
- Koekemoer, A. M., et al. 2007, *ApJS*, 172, 196
- Misgeld, I., & Hilker, M. 2011, *MNRAS*, 414, 3699
- Muzzin, A., et al. 2013, *ApJ*, 777, 18
- Naab, T., Johansson, P. H., & Ostriker, J. P. 2009, *ApJ*, 699, L178
- Newman, S. F., et al. 2012, *ApJ*, 761, 43
- Peralta de Arriba, L., Balcells, M., Falcón-Barroso, J., & Trujillo, I. 2014, *MNRAS*, 440, 1634
- Poggianti, B. M., Moretti, A., Calvi, R., D’Onofrio, M., Valentinuzzi, T., Fritz, J., & Renzini, A. 2013, *ApJ*, 777, 125
- Saglia, R. P., et al. 2010, *A&A*, 524, A6
- Sargent, M. T., et al. 2007, *ApJS*, 172, 434
- Saulder, C., Mieske, S., Zeilinger, W. W., & Chilingarian, I. 2013, *A&A*, 557, A21
- Saulder, C., van den Bosch, R. C. E., & Mieske, S. 2015, *ArXiv e-prints*
- Scoville, N., et al. 2007, *ApJS*, 172, 1
- Sersic, J. L. 1968, *Atlas de galaxias australes (Observatorio Astronomico, Universidad Nacional de Cordoba)*
- Shen, S., Mo, H. J., White, S. D. M., Blanton, M. R., Kauffmann, G., Voges, W., Brinkmann, J., & Csabai, I. 2003, *MNRAS*, 343, 978
- Shih, H.-Y., & Stockton, A. 2011, *ApJ*, 733, 45
- Simard, L., et al. 2002, *ApJS*, 142, 1
- Stoughton, C., et al. 2002, *AJ*, 123, 485
- Taylor, E. N., Franx, M., Glazebrook, K., Brinchmann, J., van der Wel, A., & van Dokkum, P. G. 2010, *ApJ*, 720, 723
- Toft, S., et al. 2007, *ApJ*, 671, 285
- Treu, T., Ellis, R. S., Liao, T. X., & van Dokkum, P. G. 2005, *ApJ*, 622, L5
- Trujillo, I., Cenarro, A. J., de Lorenzo-Cáceres, A., Vazdekis, A., de la Rosa, I. G., & Cava, A. 2009, *ApJ*, 692, L118
- Trujillo, I., Conselice, C. J., Bundy, K., Cooper, M. C., Eisenhardt, P., & Ellis, R. S. 2007, *MNRAS*, 382, 109
- Valentinuzzi, T., et al. 2010, *ApJ*, 712, 226
- van de Sande, J., Kriek, M., Franx, M., Bezanson, R., & van Dokkum, P. G. 2014, *ApJ*, 793, L31
- van der Wel, A., Bell, E. F., van den Bosch, F. C., Gallazzi, A., & Rix, H.-W. 2009, *ApJ*, 698, 1232
- van der Wel, A., et al. 2014, *ApJ*, 788, 28
- van Dokkum, P. G., et al. 2008, *ApJ*, 677, L5
- . 2010, *ApJ*, 709, 1018
- Wellons, S., et al. 2014, *ArXiv e-prints*
- Zirm, A. W., et al. 2007, *ApJ*, 656, 66

TABLE 1
SAMPLE PROPERTIES

Redshift	σ [km s ⁻¹]	R_e [kpc]	$\log(L_{e,g})$ [L_\odot pc ⁻²]	$\log(M_*)$ [M_\odot]	$(g-z)_{rest}$	D_n4000
0.218	199	6.83	2.35	11.25	1.42	1.86
0.310	170	9.09	2.12	11.45	1.74	1.68
0.346	290	16.00	1.96	11.68	1.47	1.73
0.219	305	4.90	2.76	11.41	1.47	1.77
0.349	254	6.24	2.55	11.40	1.44	1.67
0.349	290	2.83	3.16	11.25	1.47	1.72
0.345	359	7.22	2.40	11.65	1.64	1.67
0.376	221	7.11	2.50	11.45	1.43	1.80
0.228	233	6.48	2.50	11.42	1.43	1.86
0.359	360	7.82	2.40	11.51	1.49	1.75
0.220	196	3.99	2.92	11.30	1.39	1.78
0.222	223	4.15	2.70	11.20	1.52	1.73
0.349	269	7.53	2.54	11.53	1.44	1.75
0.347	304	3.78	2.95	11.35	1.50	1.94
0.347	252	6.86	2.52	11.67	1.59	1.74
0.364	230	5.67	2.67	11.46	1.39	1.64
0.696	300	3.87	3.22	11.45	1.28	1.68
0.363	319	2.82	3.13	11.21	1.43	1.74
0.308	233	8.03	2.29	11.39	1.46	1.86
0.415	222	6.71	2.55	11.51	1.39	1.82
0.578	254	3.71	3.15	11.60	1.44	1.85
0.555	195	4.60	2.89	11.46	1.31	1.61
0.436	251	6.41	2.65	11.50	1.31	1.65
0.322	211	3.27	3.01	11.10	1.43	1.83
0.348	249	4.57	2.66	11.14	1.41	1.77
0.515	306	2.74	3.39	11.50	1.37	1.68
0.680	405	3.28	3.32	11.05	1.12	1.69
0.697	259	2.84	3.50	11.50	1.16	1.47
0.530	261	4.85	2.82	11.45	1.40	1.83
0.525	148	6.87	2.53	11.39	1.26	1.90
0.670	107	3.17	3.38	11.24	1.17	1.53
0.527	310	4.94	2.74	11.40	1.34	1.89
0.218	141	2.75	2.75	10.70	1.26	1.36
0.361	277	4.38	2.71	11.30	1.50	1.85
0.667	316	6.07	2.66	11.10	1.19	1.52
0.520	173	3.21	3.00	11.05	1.26	1.68
0.623	368	3.13	3.43	11.55	1.31	1.81
0.561	218	3.82	3.23	11.19	1.14	1.55
0.528	288	7.95	2.62	11.70	1.35	1.73
0.361	235	3.91	2.78	11.30	1.54	1.64
0.360	234	3.69	2.94	11.30	1.37	1.65
0.352	344	4.30	2.64	11.24	1.64	1.79
0.220	267	4.21	2.78	11.30	1.43	1.75
0.528	269	9.05	2.39	11.40	1.23	1.59
0.425	236	3.82	2.76	11.20	1.37	1.56
0.348	297	5.05	2.65	11.45	1.48	1.79
0.265	225	4.98	2.68	11.35	1.51	1.68
0.425	253	9.81	2.29	11.55	1.40	1.83
0.531	84	3.83	2.79	11.21	1.36	1.75
0.746	255	7.99	2.85	11.75	1.30	1.51
0.350	295	4.01	2.76	11.38	1.53	1.74
0.528	227	5.58	2.68	11.45	1.36	1.75
0.662	328	3.89	3.12	11.25	1.27	1.55
0.526	123	5.54	2.56	11.16	1.26	1.65
0.467	265	4.22	2.94	11.44	1.29	1.79
0.467	292	6.49	2.71	11.55	1.51	1.79
0.631	322	1.18	4.23	11.60	1.39	1.65
0.532	186	3.33	3.12	11.33	1.25	1.74
0.516	138	4.39	2.85	11.26	1.29	1.59
0.362	218	3.01	3.05	11.20	1.41	1.66
0.502	299	6.46	2.85	11.67	1.31	1.76
0.569	301	6.62	2.75	11.60	1.37	1.50
0.595	262	3.26	3.23	11.41	1.39	1.49
0.530	199	4.04	2.87	11.29	1.33	1.67
0.535	186	11.03	2.14	11.45	1.51	1.49
0.536	191	5.11	2.74	11.40	1.34	1.72
0.378	207	2.19	3.06	11.05	1.49	1.62
0.482	130	3.20	2.89	10.93	1.32	1.46
0.412	259	4.46	2.62	11.20	1.35	1.70
0.487	207	10.28	2.07	11.20	1.31	1.61
0.393	254	1.52	3.28	10.67	1.39	1.83
0.492	269	5.89	2.66	11.54	1.37	1.66
0.270	144	4.19	2.34	10.57	1.34	1.93
0.477	219	7.37	2.42	11.43	1.32	1.62

TABLE 1 — *Continued*

Redshift	σ [km s ⁻¹]	R_e [kpc]	$\log(I_{e,g})$ [L_\odot pc ⁻²]	$\log(M_*)$ [M_\odot]	$(g-z)_{rest}$	D_n4000
0.492	288	5.63	2.71	11.37	1.35	1.77
0.550	272	2.71	3.41	11.12	1.20	1.59
0.351	241	6.42	2.50	11.15	1.41	1.68
0.667	286	3.97	3.04	11.27	1.28	1.68
0.502	243	13.38	2.19	11.65	1.36	1.77
0.517	283	3.60	2.99	11.32	1.38	1.81
0.517	228	3.14	3.14	11.38	1.33	1.67
0.518	191	10.90	2.02	11.25	1.28	1.85
0.267	275	4.71	2.60	11.32	1.56	1.80
0.654	358	2.42	3.46	11.24	1.24	1.72
0.463	210	3.89	2.84	11.24	1.31	1.59
0.248	207	3.73	2.92	11.33	1.42	1.82
0.619	187	5.08	2.94	11.05	1.14	1.66
0.349	309	3.57	3.12	11.60	1.42	1.89
0.673	138	6.48	2.67	11.26	1.26	1.67
0.361	254	6.49	2.25	11.30	1.65	1.85
0.608	204	5.03	2.95	11.62	1.42	1.60
0.345	286	10.50	2.30	11.60	1.42	1.80
0.310	366	4.86	2.72	11.48	1.49	1.75
0.372	242	5.27	2.69	11.25	1.49	1.80
0.220	209	8.95	2.22	10.95	1.33	1.44
0.354	258	7.06	2.49	11.55	1.54	1.78
0.349	292	8.98	2.66	11.85	1.45	1.69
0.503	156	4.12	3.15	11.62	1.34	1.62
0.340	365	4.02	2.90	11.39	1.48	1.69
0.323	395	9.04	2.51	11.76	1.52	1.74
0.221	251	8.83	2.34	11.50	1.45	1.79
0.373	193	12.28	2.18	11.61	1.46	2.11
0.372	269	5.46	2.73	11.45	1.44	2.14
0.213	174	5.02	2.49	11.05	1.32	1.68
0.326	238	3.31	2.93	11.05	1.43	1.65
0.467	309	4.97	2.88	11.55	1.48	1.88
0.494	424	2.59	3.69	11.75	1.28	1.65
0.473	251	6.46	2.57	11.40	1.38	1.70
0.726	299	6.61	2.95	11.82	1.36	1.65
0.467	304	3.58	3.03	11.35	1.34	1.68
0.608	216	3.32	3.05	11.16	1.38	1.69
0.515	198	3.44	3.08	11.50	1.39	1.77
0.439	280	4.76	2.93	11.59	1.32	1.65
0.564	250	6.73	2.62	11.35	1.36	1.66
0.221	230	3.59	2.94	11.40	1.50	1.78
0.425	182	4.60	2.50	11.05	1.36	1.38
0.374	431	2.90	3.37	11.47	1.40	1.71
0.599	334	4.02	3.17	11.60	1.33	1.56
0.347	237	7.45	2.26	11.04	1.36	1.75
0.350	254	3.55	2.80	11.10	1.44	1.76
0.349	270	3.42	2.84	11.08	1.46	1.76
0.371	257	5.72	2.66	11.40	1.40	1.62
0.345	232	7.69	2.36	11.37	1.39	1.73
0.480	222	6.15	2.64	11.50	1.37	1.59
0.360	216	3.09	2.77	11.07	1.40	1.81
0.552	288	3.66	3.09	11.03	1.10	1.46
0.674	256	5.53	2.88	11.50	1.25	1.55
0.480	142	4.06	2.72	10.90	1.32	1.60
0.482	330	6.94	2.70	11.70	1.37	1.75
0.496	289	3.77	3.24	11.39	1.30	1.74
0.373	192	7.37	2.24	11.25	1.53	1.53
0.550	261	7.08	2.73	11.65	1.46	1.69
0.510	183	3.47	2.96	11.07	1.32	1.84
0.346	238	5.72	2.51	11.35	1.47	1.74
0.491	302	4.71	2.77	11.40	1.38	1.62
0.407	255	3.69	2.63	11.00	1.35	1.61
0.534	272	4.80	2.71	11.15	1.26	1.38
0.344	265	5.66	2.52	11.26	1.48	2.00
0.247	236	6.02	2.60	11.30	1.41	1.46
0.218	226	4.87	2.50	11.10	1.59	1.74
0.504	252	6.91	2.68	11.60	1.41	1.93
0.349	281	5.17	2.60	11.50	1.67	1.75
0.502	201	3.35	2.95	11.18	1.32	1.90
0.674	304	3.11	3.36	11.60	1.32	1.74
0.330	219	2.94	2.95	11.06	1.47	1.80
0.348	268	4.14	2.84	11.44	1.43	1.81
0.217	220	4.89	2.40	11.13	1.62	1.77
0.534	264	3.95	2.93	11.25	1.26	2.00
0.372	233	5.38	2.71	11.20	1.40	2.05
0.521	286	3.70	2.93	11.40	1.39	1.72

TABLE 1 — *Continued*

Redshift	σ [km s ⁻¹]	R_e [kpc]	$\log(I_{e,g})$ [L_\odot pc ⁻²]	$\log(M_*)$ [M_\odot]	$(g-z)_{rest}$	D_n4000
----------	-----------------------------------	----------------	---	------------------------------	----------------	-----------

NOTE. — An electronic version of these data is available from HJZ upon request.